Curlometry Limitations on Cluster Data in the Ring Current Region

T. B. Keebler[1], M. W. Liemohn[1]

[1] Department of Climate and Space Sciences and Engineering, University of Michigan, Ann Arbor, MI.

Corresponding author: Timothy Keebler (tbkeeble@umich.edu)

In preparation for/Submitted to Journal of Geophysical Research Space Physics

Key Points:

- Ring current densities computed from Cluster II data are inconsistent with literature estimates from plasma moments.
- Examination of Cluster curlometer output shows strong evidence of contamination by linearization errors in the ring current region.
- The curlometer technique has highly constrained utility in the inner magnetosphere that requires careful analysis.

AGU Index Terms:

- 2730 Magnetosphere: inner
- 2778 Ring current
- 2794 Instruments and techniques
- 7833 Mathematical and numerical techniques (0500, 3200)

Keywords:

Ring Current, Cluster II, Curlometer

Abstract

During its ongoing mission, the Cluster II constellation has provided the first small-scale multipoint measurements of the space environment, and dramatically advanced scientific understanding in numerous regimes. One such region is the Earth's inner magnetospheric ring current, which could now be computed using the curl of the magnetic field over a spacecraft tetrahedron instead of plasma moments. While this produced the first 3D current estimates, it also dramatically contradicted prior ring current studies with differing magnitudes and correlations with storm indices/local times. In this analysis, we revisit Cluster ring current data via curlometry, and conduct additional sensitivity simulations for the first time using actual spacecraft position data. During the orbits that observed ring current structure, tetrahedron shape and linearity assumptions can create large errors up to 100% in curlometer output that contradict accepted estimated quality parameters. Furthermore, the plasma gradients computed from JxB are distinctly different from those measured via plasma particle measurements, and are also contrary to theorized plasma structure. A new climatology of the ring current is then presented, but with severe limitations that are explicitly defined. Thus, the discrepancies are addressed by improved curlometer uncertainty estimates.

Plain Language Summary

The ring current is a structure in near-Earth space that causes magnetic changes on the Earth's surface and is very important for plasma transport as well. Previously, it has been measured using single spacecraft by sampling the electrically charged gases. However, the Cluster mission allowed the ring current to be calculated in greater detail by observing magnetic fields, which are easier to measure. This technique was dubbed the 'curlometer,' and has applications in many regions. For the ring current region in particular, the curlometer technique produces very different ring current strengths than the particle-measurement methods. To resolve this, we reevaluated the curlometer technique and tested it against simulated data for which the current can be analytically calculated, showing larger uncertainty than previously thought. Thus, the curlometer may not be a useful technique for the Cluster mission to measure the ring current. All data from the near-Earth portions of the mission were then reanalyzed and a new picture of the ring current emerged that had better estimates of limitations.

1. Introduction

The Cluster II multi-spacecraft mission, launched in 2000, has been a resounding success in probing a multitude of environments by collecting data in varying three-dimensional configurations. By providing multipoint measurements, Cluster benefits from improved calibration and novel techniques that cannot be implemented by a single spacecraft (Paschmann & Daly, 2000). One such technique has been dubbed the 'curlometer,' because it uses the four spacecraft as vertices of a tetrahedron to compute the linearized gradient of magnetic field and find the average current density in the tetrahedron volume (Dunlop et al., 1988). Although requiring limitations and assumptions, the curlometer technique has been applied to many regions containing magnetic structure that is characteristically larger than the tetrahedron (Dunlop et al., 2016). Thus, we have gained additional insight into the three-dimensional current structure of features from the cusp to the magnetotail (e.g., Henderson et al., 2008; Dunlop et al., 2015; Petrunkovich et al., 2014).

In the ring current region of the inner magnetosphere (~3-7 R_E) (Ganushkina et al., 2018), the curlometer technique has been applied to provide a better estimate of ring current magnitudes critical for understanding storm indices and current closure (also capturing field-aligned currents in this region) (Vallat et al., 2005; Zhang et al., 2011). Curlometry offers an alternative to computing current from pressure moments, which have higher uncertainty through methodology and instrumentation (Dandouras & Barthe, 2011). Pressure moments can also only yield a single component of current orthogonal to the plane defined by the spacecraft trajectory and local magnetic field, whereas curlometry provides the full current vector.

An important distinction must be made regarding the ring current. Several discrete current systems are often nebulously consolidated into the 'ring current,' including a diffusional component in 100s of keV and a convectional component inbound from the plasma sheet (see review by Ganushkina et. al, 2015). The former dominates during quiescent conditions, while the latter becomes more prominent during geomagnetic storms, is often asymmetric in local time, and contributes significantly to the Dst index (e.g., Milillo et al., 2001, 2003; Liemohn et. al, 2001a, 2001b). Hereafter, we use the term 'ring current' to signify the diffusional or quiescent component that is distinct from the plasma sheet (and its innermost extension as the convective part of the ring current).

Ring currents computed from Cluster data via curlometry suggest a westward current that varies from near zero to a few tens of nA/m^2. Vallat et al. (2005) found that the magnitude had no correlation with geomagnetic activity indicated by the Disturbance Storm Time (Dst) index, and using subsequent orbits, other papers (Zhang et al., 2011; Grimald et al., 2012; Shen et al., 2014) have built climatologies for the ring current using different thresholds for storm/quiet delineation. However, these results are contrary to plasma moment and single spacecraft magnetometer current calculations, which suggest currents approaching 10 nA/m^2 occur only near storm-times, and are consistently weaker than this value with lower activity (e.g., Lui et al., 1992; Greenspan & Hamilton, 2000; Jorgensen et al., 2004; Le et al., 2004). Furthermore, time series or radial plots of curlometer output often show structure that is inconsistent with theory; namely, near-constant current magnitude instead of an inverse relation with L-shell (assuming the pressure peak is radially inward of perigee). These discrepancies urge a thorough reanalysis of Cluster data to account for these observational differences and to probe the underlying theory and assumptions of current calculation (Liemohn et al., 2016).

2. Methodology

2.1. Implementation of the Curlometer Technique

The curlometer technique has been well-documented in numerous papers; thus, only a brief discussion is provided here. According to the Maxwell-Ampere Law, and assuming stationarity (removal of time dependence term):

$$\mu_0 \vec{J} = \nabla \times \vec{B} \qquad (1)$$

which can be rewritten with respect to a reference magnetic field vector at a reference location:

$$\vec{J} \cdot \left(\left(\vec{r}_i - \vec{r}_{ref} \right) \times \left(\vec{r}_j - \vec{r}_{ref} \right) \right) = \frac{1}{\mu_0} \left(\vec{B}_i - \vec{B}_{ref} \right) \cdot \left(\vec{r}_j - \vec{r}_{ref} \right) - \left(\vec{B}_j - \vec{B}_{ref} \right) \cdot \left(\vec{r}_i - \vec{r}_{ref} \right) \qquad (2)$$

With four spacecraft, the curl of the magnetic field can be computed by cyclically differencing over each face of the tetrahedron to find the three-dimensional linear gradients and summing (Equation 2), yielding the average current density within the tetrahedron volume. A more detailed treatment of the technique can be found in Dunlop et al. (1988) and many subsequent papers. The most explicit outline is provided by Middleton and Masson (2016).

For this study, the curlometer computation was performed by modifying a Python script provided by the Cluster Science Archive (CSA) (Laakso et al., 2010). The script was thoroughly tested for correct methodology: first with sample data provided by CSA, then by alternating reference spacecraft and perturbing parameters, and finally by 'flying' the constellation through simulated linear current environments. In each case, the script behaved as expected, demonstrating independence of reference spacecraft choice and correctly capturing the simulated currents. This analysis followed the work of Robert et al. (1998) and independently confirmed the results of that study. The code was further verified by replacing magnetic field data with constant field, correctly producing no current, with an idealized dipole field, producing insignificantly small current, and with the International Geomagnetic Reference Field (IGRF), which also created only small current outputs as expected. Thus, the curlometer script was confirmed to function correctly in a variety of environments. Extensive verification provided the necessary foundation for later conclusions by definitively verifying the curlometer computation.

Raw magnetic field data from the Fluxgate Magnetometer (FGM) instruments on each spacecraft were obtained in spin resolution, along with position data and differential particle flux from the CIS instrument suite. Temporal data resolution was experimentally determined to have only a small effect on current values, within the ranges of available datasets; therefore, spin resolution (~4 s cadence) sufficiently captures the scale of desired features. All values were converted from Geocentric Solar Ecliptic (GSE) to Solar Magnetic (SM) coordinates using the SpacePy Python package and tested to ensure they retained their magnitudes. Note that westward azimuthal current is defined to be positive. IGRF values were then subtracted from the magnetic field data to remove as much nonlinear magnetic gradient as possible and therefore allow a more robust linearity assumption and curlometry result (Dunlop et al., 2016). This has a significant effect on current densities for spacecraft separations above 300 km.

2.2. Ring Current Event Selection

The Cluster tetrahedron was most regular within the ring current region for select dates from 2001-2004. Using prior studies for guidance in event selection (Vallat et al., 2005; Zhang et al., 2011; Shen et al., 2014), six hours of data surrounding every perigee pass individually underwent visual inspection. Each case was passed through the curlometer script and examined. Cases were removed if data was missing from anywhere in the expected ring current torus, or if there were obvious errors in the data (e.g., discontinuities, asymptotes). This also entirely removed passes that experienced eclipses.

Figure 1 presents an example of the Cluster data examined for this study, specifically from the 9 May 2002 perigee pass, when the tetrahedron shape was within the nominal guidelines for yielding reasonable current densities from the curlometer technique. The top two panels show the current density, first in SM coordinates and then just the azimuthal component.

The middle shows the interspacecraft differences in magnetic field used in the curlometer calculation. The final two panels present plasma energy-time spectrograms. The higher energies (>30 keV) are measured by the Research with Adaptive Particle Imaging Detectors (RAPID) experiment (Figure 1d). Lower energies (< 40 keV) are measured by the Hot Ion Analyzer (HIA) instrument, part of the Cluster Ion Spectrometry (CIS) experiment (Figure 1e). Note that the colorscales on the two ion flux panels are logarithmic and quite different.

Several features are readily seen in Figure 1. First, there is a smooth section of current near the equator and near perigee, surrounded by intervals with highly fluctuating currents. Second, the magnetic field differences do not show a drastic change at the variable/smooth current density boundary (the red-dashed vertical lines). That is, the current densities come from rather small deviations in magnetic field differences, sometimes hardly noticeable on the plotted scales. A third feature is the existence of both hot ions and cold ions in the smooth current density region. The hot ions of the ring current have much lower flux than then cold ions of the plasmasphere, but presumably they dominate the plasma pressure and contribute most to the local azimuthal current in this region.

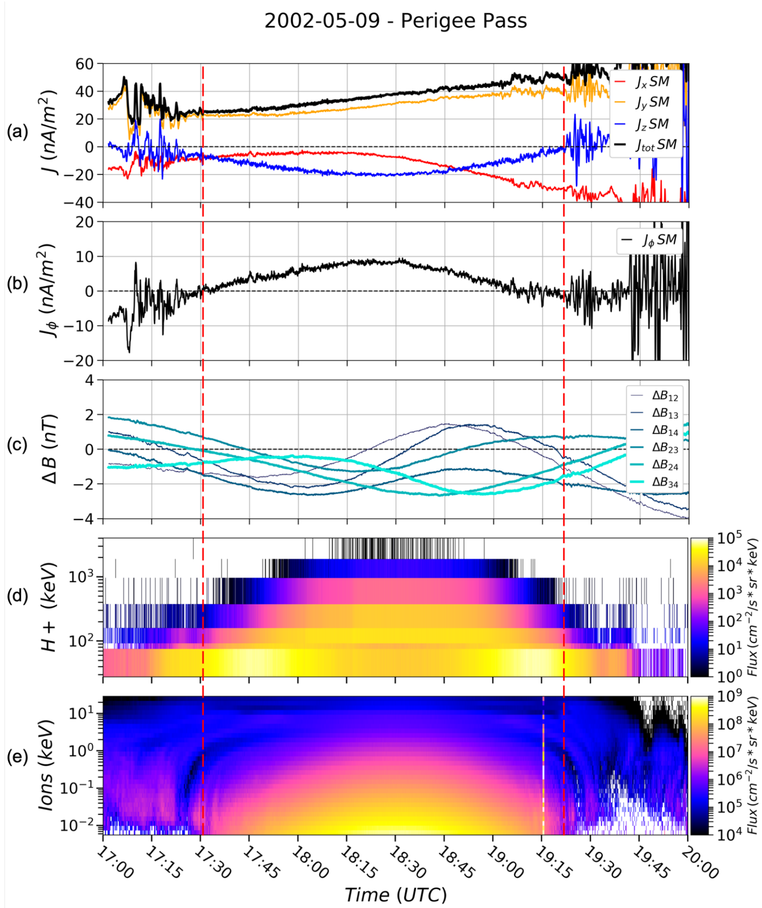

Figure 1. 9 May 2002 Perigee Pass. **a)** Curlometer current components in SM coordinates. **b)** Azimuthal current component (J_ϕ) in SM coordinates. **c)** Inter-spacecraft magnetic field differences. **d)** RAPID H+ omnidirectional differential proton flux from Spacecraft 1 (Rumba). **e)** CIS/HIA omnidirectional differential ion flux from Spacecraft 1. Dashed vertical lines estimate presumed ring current boundaries.

Each perigee pass was manually trimmed to capture and identify the ring current region. Outside the ring current zone of smooth current signatures, curlometry yields wildly oscillating current components as a result of the complex structure in these regions below the tetrahedron scale size (Vallat et al., 2005). Conversely, the presumed ring current section of the orbit is marked by a smooth timeseries indicating a homogeneous structure. Comparison with RAPID plasma data showed that particle counts and energies increased coincident with the smooth currents, and this supported our identification of the ring current region (as seen in Figures 1a, 1b, and 1d).

2.3. Comparison with Plasma Moments

Current densities can be computed from various space measurements, not only from the magnetic field but also from the plasma. Rearranging the equations to remove current density results in a formula for pressure gradient as a function of the magnetic field. Therefore, the pressure gradient computed using the curlometer result and pressure gradient from the CIS and

RAPID experiments onboard Cluster should be consistent. To compute ∇P, the cross product of the current vector and magnetic field vector was taken in Solar Magnetic (SM) coordinates.

For comparison, data from the CIS and RAPID experiments were obtained from the CSA. CIS data from both the Hot Ion Analyser (HIA) and Composition and Distribution Function (CODIF) instruments provided plasma moments for all species between ~5 eV - ~40 keV calculated by the spacecraft science team and checked for quality (Dandouras & Barthe, 2011). For the higher-energy RAPID data (~28 keV - ~4046 keV), the pressure moment was not provided but could be computed via

$$P = 4\pi(0.51767 * 10^{-8})\left(\frac{2}{3}\right)\sqrt{m}(E_{MAX} - E_{MIN})\sqrt{\frac{E_{MAX}-E_{MIN}}{2}} * I \qquad (3)$$

as given by the RAPID instrument team (Daly & Kronberg, 2013). In Equation 3, 'm' represents the mass of the species, 'I' represents the measured omnidirectional intensity, and 'Emax'/'Emin' are the bounds of the energy channel.

Computing the spatial gradient of pressure was limited by the geometric positions of the spacecraft and the availability of datasets; in many cases, plasma data was only available from one or two spacecraft, or they operated in different modes that prohibit comparison across the tetrahedron. Additionally, plasma data is fraught with uncertainty, and for the purpose of this study should be treated cautiously. For these reasons, the spatial gradient was only taken along the orbit of one spacecraft (dP/ds) using the assumption of stationarity.

Use of plasma data requires caution because of many limiting factors. Note that the instruments on Cluster measure only a portion of the complete energy spectrum, and require extensive data processing to produce meaningful information. The data used in this study have already been processed by the respective instrument teams to account for things like detector areas and look directions, which necessarily involve approximations to get a full integrated flux.

2.4. Nonlinear Current Simulations and Tetrahedron Shape

To investigate the performance of the curlometer in different environments, simplified simulations were used to probe for error. When testing curlometry through simulated magnetic fields, deviation from linear magnetic gradient causes errors in the output current. Robert et al. (1998) suggests that this effect is <10% for a regular tetrahedron with elongation and planarity both below 0.8 (see Paschmann & Daly (1998), Chapter 13, for detailed treatment of tetrahedron geometric parameters). However, a comparison between idealized current input and curlometer output has not been conducted using actual spacecraft position data. This process is distantly similar to that of Dunlop et. al (2002), but uses a more idealized situation and a more focused region of interest.

To represent the simulated currents, an infinite slab current sheet was constructed with thickness scaled to the selected perigee pass and quadratic variation from 0 nA/m^2 at the boundaries to 10 nA/m^2 at the center; the slab was then offset to the center of the selected spacecraft flight track. Although oversimplified, this model creates gradients consistent with structural understanding of the magnetosphere (eg. Le et al., 2004). Using the Biot-Savart law, the magnetic field vectors were computed at each spacecraft location, then passed through the curlometer script. A simplified visualization is provided in Figure 2, depicting the spacecraft trajectory, variation of current, and magnetic field for a single case.

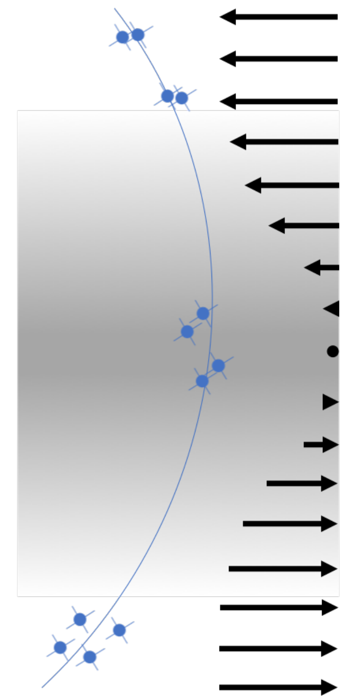

Figure 2. Simulated Current Scheme. Arrows denote magnetic field. Shading indicates quadratically-varying current density (out of page). Simplified spacecraft flight track and tetrahedron evolution are shown.

Because the Cluster tetrahedron had some degree of irregularity near perigee on all orbits, the simulated current sheets were iterated through all orientations and current directions. Additionally, for each current orientation, the tetrahedron was rotated about the barycenter and reanalyzed to deduce the combined effect of current direction and tetrahedron aspect.

It became immediately apparent that the production of false current components occurs in the same plane as the simulated current, and in the direction that has magnetic field in common with the simulated current. In other words, the false current produced is parallel to the magnetic field gradient. For example, a simulated current in the J_Z direction centered in the x = 0 plane creates a false current in the J_X direction. Proportionality, however, is not so direct because the magnitude of the false current evolves with gradient magnitude, nonlinearity, and tetrahedron geometric factors.

3. Results

3.1. Observed Current Structures

Figure 3 provides a representative sample of a single perigee pass, from 10 October 2003. While the observed current structures varied widely across the total dataset, this event provides a typical case that shows common trends and avoids extremes. The top panel shows curlometer output in SM Cartesian current components, with the components clearly diverging later in the flight track. The next panel displays the azimuthal current component computed from the Cartesian output. These current values are then compared to the quality parameter Q and the tetrahedron geometry in the form of elongation and planarity. Note that the geometrics are plotted on separate y-axes to capture detail. The plot limit times have been chosen to roughly coincide with the RAPID plasma data (not shown) as a means for identifying the region of interest.

For this inner-magnetospheric traversal, a few key features immediately stand out. The Cartesian current components quickly diverge near the end of the flight track (Figure 3a), which in turn causes the azimuthal current component to develop a strong negative trend (Figure 3b). This is clearly nonphysical behavior, and cannot be trusted to accurately represent the ring current. The large uncertainty in the data is corroborated by the calculation of Q, which is only below the standard threshold of 0.5 in the beginning of the flight track (Figure 3c). However, even during periods of relatively high confidence, the currents are still diving towards negative values. A potential explanation for the diverging current lies in the tetrahedron geometry (Figure 3d), which has a high elongation ($E > 0.8$) and an increasing planarity (from $P < 0.4$ to $P = 1$) where low values are more regular and desirable.

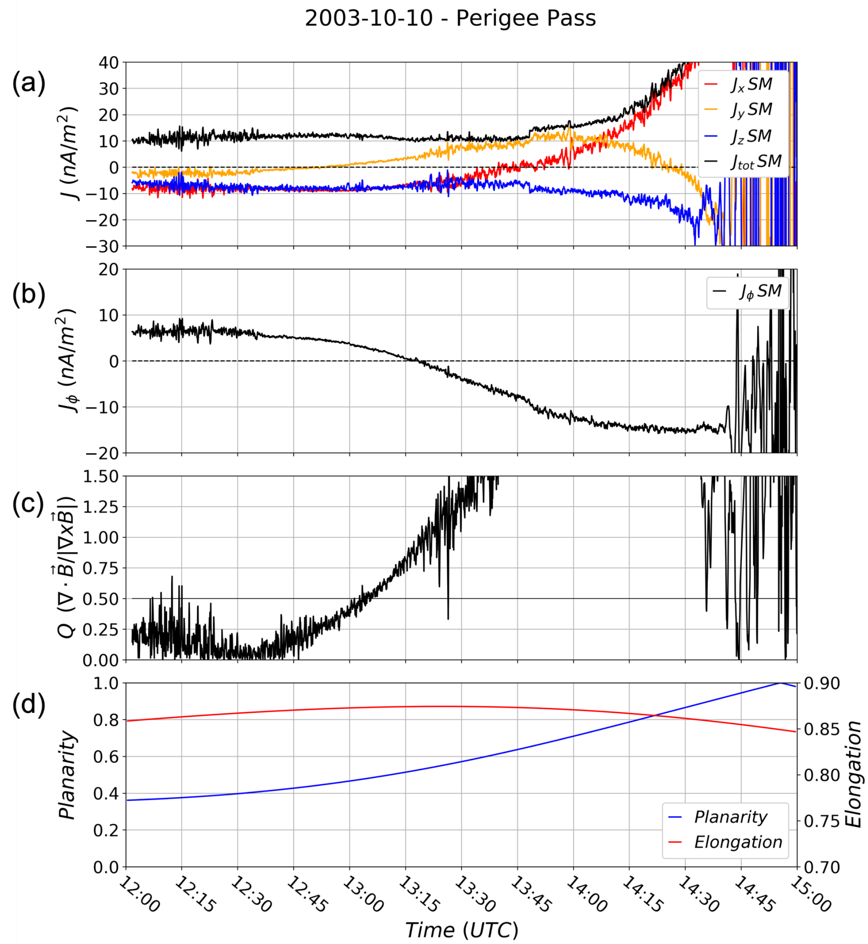

Figure 3. 10 October 2003 Perigee Pass. **a)** Cartesian current components in SM coordinates, showing clear divergence after perigee. **b)** J_ϕ with a clear sloping profile. **c)** Quality parameter Q, satisfying the Q<0.5 threshold until just after 13:00. This is not centered on the ring current region. **d)** Tetrahedron shape parameters elongation and planarity. Note that planarity is steadily increasing to unity throughout the ring current traversal.

In all orbits where Cluster achieved relatively regular tetrahedra when traversing the ring current region, curlometry results varied greatly in structure and magnitude. Nearly all passes had azimuthal current components in a westward direction with a magnitude peaking at or below 10 nA/m^2. The tetrahedron did not pass into eastward current in most orbits, with eight ambiguous exceptions. From these cases, the apparent eastward current reversal was situated at a maximum of L = 4.7 R_E; however, uncertainties in position and magnitude preclude definitive claims of eastward current. Otherwise, Cluster perigee was insufficiently low to capture the reversal.

Current data also showed large cross-hemisphere field-aligned currents (FACs), around 10 nA/m^2 in Figure 3a on 10 October 2003. The largest FACs are in excess of 20 nA/m^2 in perigee passes from 2002, and FACs in most other orbits were southward at ~5 nA/m^2 and did not vary significantly between hemispheres. This ubiquity and consistency of a southward FAC, regardless of geomagnetic activity, latitude, or local time, is curious and will be explored later in this study.

Of particular interest is the structure of the azimuthal current. In many of the cases, there is a clear negative trend in the Northern Hemisphere as the spacecraft passes perigee, and the current quickly becomes decisively negative. The signature of azimuthal current thus translates to a westward current south of the equator and eastward current north of the equator. This is entirely inconsistent with our understanding of physical current structures (Ganushkina et al., 2018), and calls the curlometer result into serious doubt. Data from 2003-2004 is especially susceptible to the negative trend, where the tetrahedron evolves to higher planarity. The slope of this trend varies irregularly between consecutive orbits, and therefore cannot be effectively detrended. Despite this unpleasantry, most orbits show expected symmetry in the structure of the ring current that is characterized by two local maxima on either side of the equator. Physically, these peak azimuthal current values indicate the maximum pressure gradient, suggesting that the spacecraft are Earthward of the maximum gradient but have not reached the pressure peak (where current reverses and becomes eastward) (eg., Lui et al., 1987; Ganushkina et al., 2018). The curlometer, therefore, seems to capture some relative structure but not magnitude.

3.2. Plasma Pressure Discrepancy

Keeping in mind the many limitations (for example, incomplete spectra, detector absolute calibration uncertainties, integration techniques, etc.), pressure gradients computed via curlometry and those observed directly nevertheless show distinct inconsistencies that are difficult to reconcile. The quality and availability of the plasma data constrains the efficacy of the comparison, but provides a rough estimate of plasma gradient magnitude and structure.

In the selected sample case from 9 May 2002 shown in Figure 4, curlometer output is compared with onboard plasma measurements from Spacecraft 1 (Rumba). The first panel shows the curlometer-based JxB, which can be directly compared to the measured pressure gradients (dP/ds) from CIS and RAPID observations in the second panel. For reference, plasma pressures are provided in Figure 4c, so that the physical structure of the plasma becomes apparent. H^+ pressure gradients in Figure 4b (red) are computed from the pressures in Figure 4c.

The observed plasma data clearly show a maximum pressure within the perigee pass ($\nabla P = 0$), while the curlometer-derived pressure gradient only suggests a maximum of P_z and not P itself. The z-component of the curlometer pressure gradient changes sign near the equator; this suggests that the current is centered near the equatorial plane, matching results from Vallat et al. (2005). Plasma gradient magnitude along the flight track shows a more distinct reversal near the equator, as the spacecraft approaches and then retreats from a pressure maximum. In this case, it is presumed that the spacecraft is still within the main body of the ring current because the gradient profile only intercepts once.

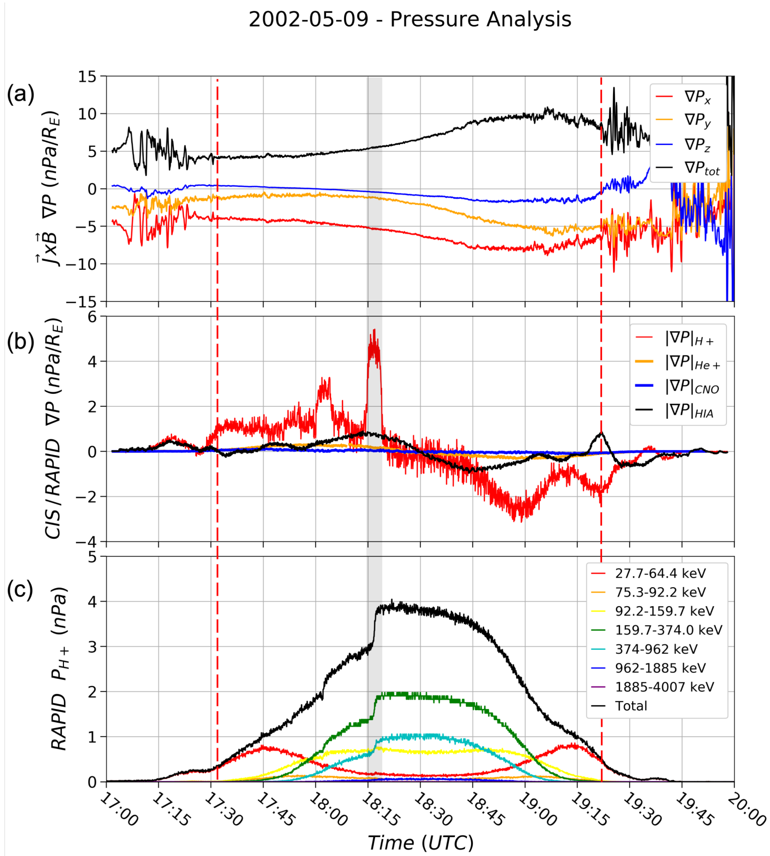

Figure 4. a) Pressure gradient components from curlometer result JxB. **b)** Pressure gradients from plasma data. These gradients are computed along the flight track, dP/ds, to capture the maximum discernable gradient. The pressure data is provided by CSA omnidirectionally, and there is some overlap between HIA and the RAPID H^+ (~5 eV – 4007 keV). Note a small error in all pressure channels (c) that causes the spike in gradient at 18:15, highlighted in gray shading. **c)** Partial pressure from RAPID proton fluxes by channel.

Curlometry provides a gradient magnitude increasing from 5 nPa/Re to 10 nPa/Re throughout the traversal. However, the total measured pressure gradient summed over all energy channels never exceeds 4 nPa/Re, excepting the discontinuity at approximately 18:15. The smallest curlometer-derived pressure gradient is therefore greater than the steepest plasma-derived gradient, which is a significant departure that questions the validity of the computations. In addition to this difference in magnitude, the shapes of the pressure gradients are incredibly dissimilar. The curlometer-derived pressure gradient peaks in the Northern Hemisphere, as opposed to the HIA/RAPID approximate symmetry. Figure 4 provides a representative sample of the ring current dataset; most orbits with available data show the same troubling discrepancies and structure but have noisier data. The consistent shape of the curlometer-derived pressure gradients between orbits suggests that they are influenced greatly by geometric factors that recur at each perigee pass.

Prior analyses suggested that a current-carrying population evades ion spectrometers and thus inflates the current density (see, for example, the discussion of Vallat et al., 2005). The combined CIS/RAPID detectors have a large energy range, and it is unlikely that they are missing a large enough particle population to account for the curlometer currents, especially considering the consistency of differences between perigee passes. Given the observed structure discrepancy, it seems more likely that the curlometer values are in error.

3.3. Curlometer Dependence on Tetrahedron Orientation

As discussed in the methodology section above, idealized current configurations were used to replace the observed Cluster magnetometer data with simulated data, for which the corresponding current density is known. Figure 5 shows the results of an idealized current sheet centered in the z = 0 plane. The current sheet varies quadratically from J = 0 at the boundaries to a maximum in the center of 10 nA/m^2. The tetrahedron was 'flown through' the simulation using actual position data from 10 October 2003 and replacing the magnetic field (Figures 5a-5c). Then, the tetrahedron was rotated about its barycenter and the x-axis by 90° to produce the lower portion (Figures 5d-5f). For each orientation, the curlometer output (Figures 5a and 5d) is compared to Q (Figures 5b and 5e) with the 0.5 threshold labeled (vertical red lines). Both the curlometer output and the imposed current density are plotted. To the right of each current plot, the tetrahedron shape in the midpoint of the perigee pass is plotted in barycentric coordinates (Figures 5c and 5f). The J, ∇B, and planarity are depicted by arrows. Note that the planarity vector shows the direction of the largest semiaxis, instead of the planarity normal direction.

It is immediately apparent that, despite the simulated current being purely in the J_y direction, a large false current is output by the curlometer technique. In this instance, the false current grew as large as 5 nA/m^2 in the J_z direction (Figure 5a). The unaltered tetrahedron orientation produced nearly the greatest false currents of any orientation. Furthermore, the large false currents occur well below the $Q < 0.5$ quality standard, with significant stature even at more stringent thresholds. Rotating the tetrahedron about its barycenter produced different results. Instead of a large false current, the same tetrahedron parameters with a quarter rotation captured the currents remarkably well, and Q is much lower throughout the pass. All else equal, rotation dramatically changed the output by altering the planar direction with respect to the magnetic field gradient. When rotated farther, currents appear again, related to the orientation of magnetic gradient with respect to planar direction. Larger false currents are produced when the largest planar semiaxis is close to parallel with to the magnetic gradient; this can be seen in Figures 5c and 5f. The tetrahedron was rotated independently and in combination of all three axes, with the largest changes highlighted in the figure. Rotation about other axes produced smaller false currents, so the uncertainty contributions from those axes are smaller. It seems that false currents are directly related to the length of the tetrahedron semiaxis parallel to the magnetic gradient; therefore, some rotations will roughly preserve that quantity.

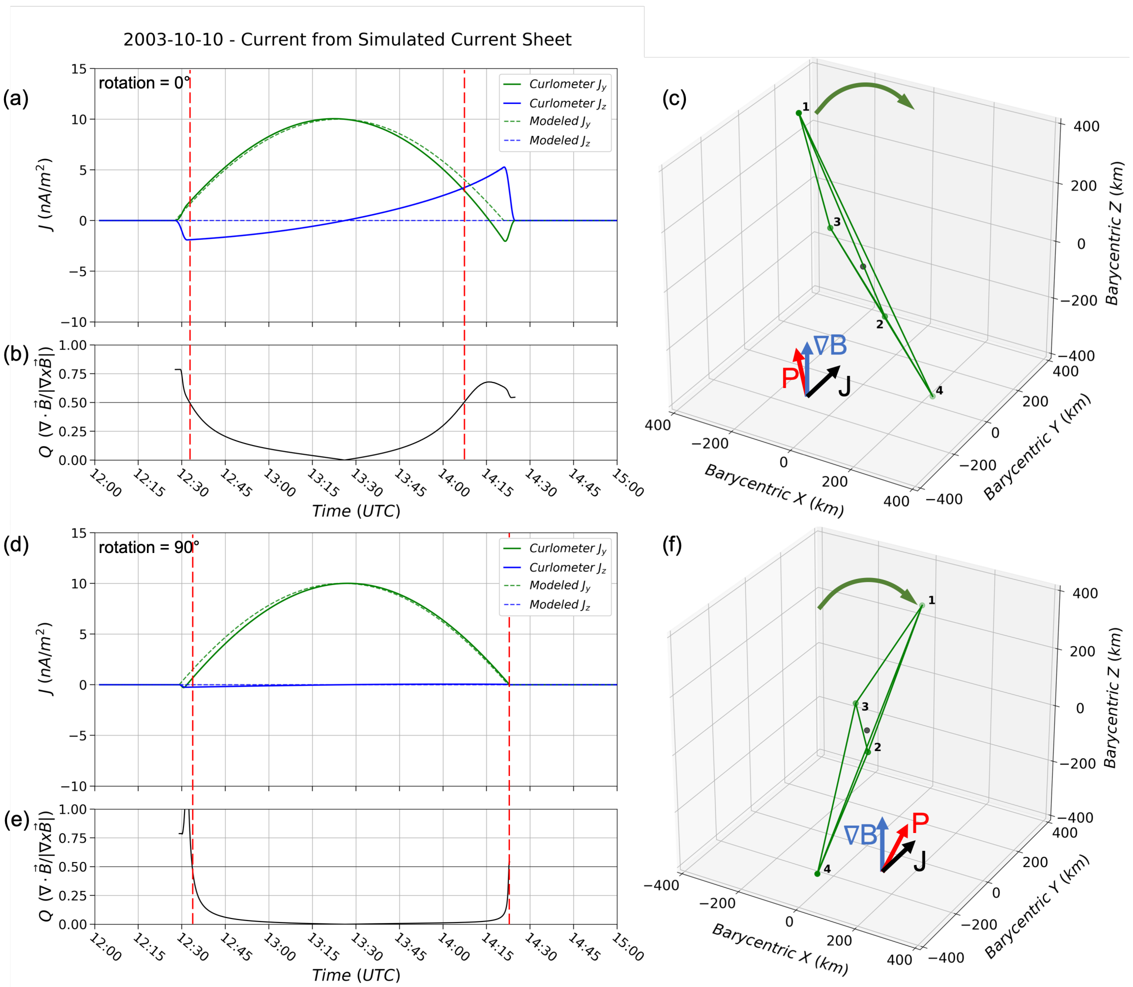

Figure 5. Quadratically varying infinite current sheet centered on the z=0 plane using the orbit spatial parameters from 10 October 2002. From unaltered flight track position data: **a)** Curlometer output. **b)** Quality parameter Q. **c)** Tetrahedron shape and pertinent vectors. For **d) - f)**, the current sheet remained the same, but the tetrahedron was rotated about the barycenter by 90°, pivoting clockwise around the x-axis. Red dashed lines denote the region with Q < 0.5. The black arrow 'J' depicts the direction of simulated current. The blue arrow '∇B' shows the gradient of magnetic field. The red arrow 'P' shows the orientation of the longest tetrahedron semiaxis.

Using the same methodology as Figure 5, curlometer output from actual position data and modeled current sheets in all orientations produced large non-physical currents in complementary components in nearly all cases. These false currents are in the direction of the magnetic gradient associated with the magnetospheric current sheet (like the spurious Jz in Figure 5a), but the magnitude was highly dependent on tetrahedron orientation and shape parameters. Even satisfying the Q < 0.5 threshold, false currents were calculated to be as much as 100% of the imposed current, with significant implications that ring current curlometry can be wildly inaccurate despite accepted data filtering methods.

Rotating the tetrahedron about the barycenter provided additional insight into the relationship between shape, orientation, and false current. Elongation was consistently near 0.8 for all passes and timestamps, but planarity evolved quickly from 0.4 to near unity in the few hours surrounding perigee. Thus, planarity was observed to have the larger effect of the shape parameters, and maximum false current was produced by a largest planarity semiaxis that was close to being parallel to ∇B and therefore experiencing the largest linearization error. In cases with multiple gradients, false and physical currents added linearly through the curlometer, requiring understanding of physical currents to deduce the false components. However, false current was also strongly related to nonlinearity in magnetic gradient, so without quantitative knowledge of this it is impossible to correct in-situ data for these differences. Numeric correction of curlometer output requires additional study and technique development and will be severely limited by enhanced stationarity assumptions.

4. Climatology

4.1. Representative Curlometry

The high-sensitivity of curlometry under simulated currents comparable to the ring current, combined with the suspicious negative trending of current data and large FACs, suggests that this methodology has severely limited utility under these conditions. Furthermore, the complexity of the magnetosphere shrouds attempts to separate physical currents from computation artifacts. Thus, careful event selection, removing most cases, is critical to analysis integrity.

Previously, the quantity $Q = \mathrm{div}(B)/\mathrm{curl}(B)$ was used as a quality flag, with values less than 0.5 considered acceptable uncertainty. However, simulated currents can produce false results with the same order of magnitude as the imposed currents even when Q is below the 0.5 threshold (as seen in Figure 5), depending on tetrahedron orientation. Orbits in the Cluster dataset each only contain a small duration under this threshold and are likely to contain larger magnitude errors outside this range. While the latitudinal extent of the ring current sheet can be established with reasonable confidence via plasma data and regularity of current profile, information regarding the magnitude and direction of the current may be grossly inaccurate. Examining tetrahedron orientation through simulated current sheets produced new maximum uncertainty estimates that exceed the E-P space plots constructed by Robert et al. (1998).

New selection criteria for suitable ring current data must examine the curlometer output in conjunction with the quality parameter Q and a priori knowledge of the magnetospheric environment to judge data validity. Data should be disregarded if it shows evidence of geometric factors affecting its timeseries, including diverging J components and asymptotes. Furthermore, only data with a maximum Q of 0.5 should be considered in climatological studies of the ring current because instances above this threshold almost certainly have large errors in both magnitude and direction. Lowering the threshold further increases confidence, but at the expense of sample size. To effectively filter curlometry output, a more complete analysis of tetrahedron and environmental parameters needs to be constructed, both through higher-degree estimates of nonlinear magnetic field gradient and the orientation with respect to the tetrahedron. Curlometer uncertainties stem not only from tetrahedron geometry, but also from the geometry in combination with the magnetic environment. Then, additional quality standards can be developed to increase trustworthiness of current calculation.

4.2. Cluster-Derived Climatologies

To establish a view of the ring current at all local times, it is important to have a large and representative sample of measurements throughout the whole precession of the Cluster orbit. This aim is hindered by the extensive data filtering required to produce meaningful curlometer results. Therefore, two climatologies are presented: the first, with all available data subject to the $Q < 0.5$ threshold, and the second with visual inspection of each event for quality and physicality. These techniques provide the best possible picture given present curlometer understanding.

When considering all unfiltered data for a climatology as a function of radial distance or magnetic latitude, no robust trend can be discerned because of the offset of perigee from the magnetic equator. Thus, the best metric is McIlwain's L-parameter. For such strong magnetic field as in the inner magnetosphere, L can be approximated using a dipolar field.

All perigee passes are considered in Figure 6. Taking data with $Q < 0.5$ and with $L < 7$ R_E, events were sorted into "storm-time" and "quiet-time" categories delineated by Dst = -25. While storm events show wild variation and sparse data coverage (Figure 6a, red data), quiet events provide insight into the radial ring current distribution (Figure 6b). The unfiltered spread of quiet data is visualized via boxplot in Figure 6b, binned by L-shell in 0.2 R_E increments. The bottom panel shows the number of observed current values in each bin. The majority of ring current observations with $Q < 0.5$ lie Earthward of $L = 5$, so conclusions in this region are more robust.

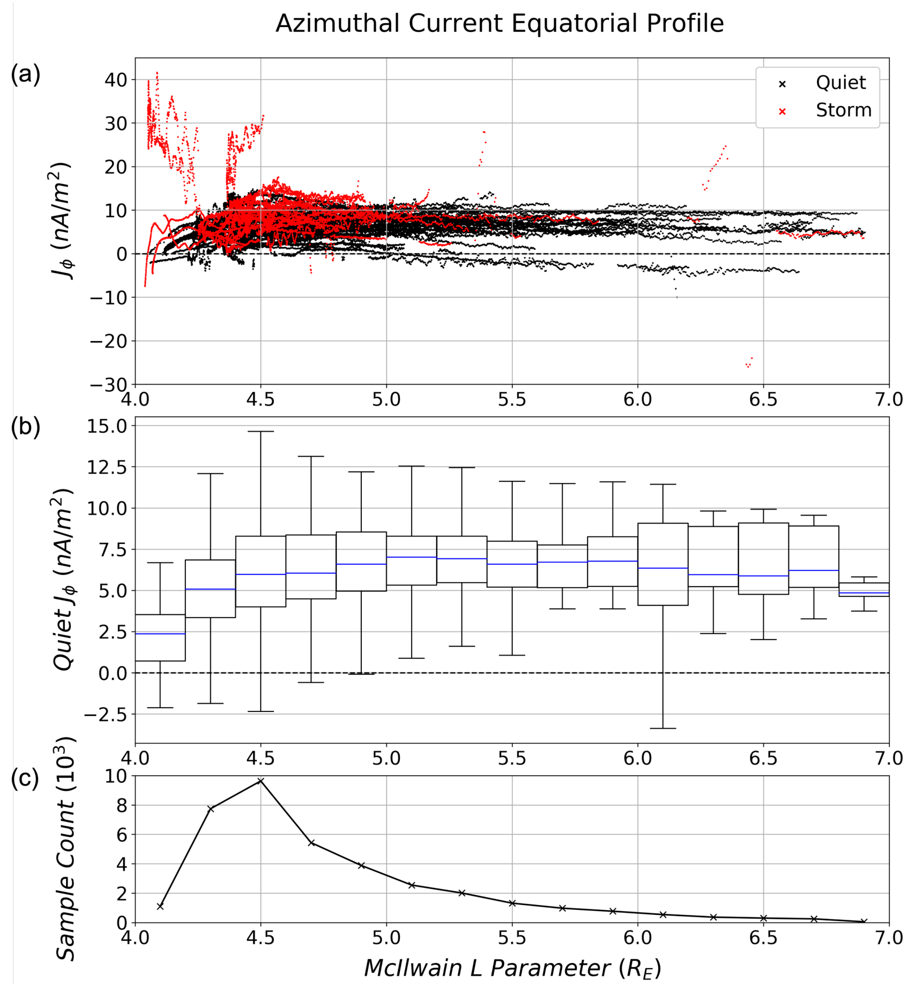

Figure 6. Ring Current Statistical Study. **a)** Azimuthal current as a function of L-shell. **b)** Quiet-time current distributions. Box heights show the median and interquartile range (IQR), box widths represent current binning with respect to L value, and vertical bars indicate values up to 1.5*IQR. **c)** Observation count per data bin.

The ring current as measured by Cluster between 2001 and 2004 was largely below 10 nA/m^2 in magnitude, with a marked decrease towards L = 4 R_E. This suggests that the eastward reversal of the ring current usually lies inside the Cluster orbit, although there is less data in this region, and agrees with prior studies (Shen et al., 2014; Vallat et al., 2005). However, at all values of L, the median of ring current magnitudes was below 7.5 nA/m^2, and the third quartile was below 10 nA/m^2, as seen in Figure 6b. This agrees with plasma pressure calculations but contradicts earlier curlometry, such as the results of Vallat et al. (2005). For disturbed magnetospheric conditions, less data were available and the scatterplot reveals higher spread (red data, Figure 6a). Cluster data does not effectively show a defined storm-time ring current structure with sufficient confidence. However, the linearization assumption becomes less robust during geomagnetic activity, because the extent of viable storm-time data is much smaller than quiet-time data (the limiting factor is usually that $Q < 0.5$ for a shorter duration).

Figure 7 visualizes a subset of the full current vectors in 3D space. The data were subjected to the quality constraint Q < 0.5 and were then binned and averaged in 15-minute intervals for clarity. The plot contains both storm-time and quiet-time data, and all local times. The J_Z component is strong in most cases, and almost always negative. In fact, the dominant current at most latitudes is southward field-aligned current. This is the first report of such large currents, and should be viewed with extreme caution. Expected FACs in this region should diverge approximately from the equator, because this is the location of the pressure peak (Ganushkina et al. 2018). Thus, the large field-aligned component provides additional evidence that the curlometer output may not be a good representation of the actual currents.

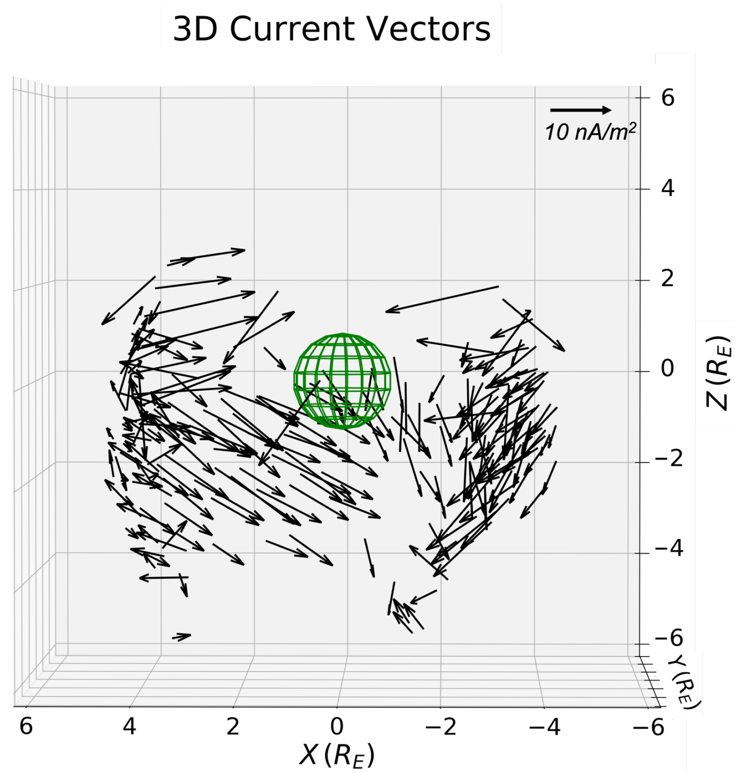

Figure 7: 3D Current Vectors. Included vectors were binned and averaged over 15-minute intervals to avoid clutter. For a top-down view depicting local time dependence, see Figure 8.

To investigate the distribution of current density as a function of local time, currents with Q < 0.5 inside L = 7 (same criteria as Figure 6) were averaged for each perigee pass; the results are provided in Figure 8. The top panel shows the full horizontal current vectors, and the bottom panel shows just the azimuthal component. Note the large radial components of current at all local times for nearly all events; this is not expected from theoretical current structure (eg., Ganushkina et al., 2018), nor has it been reported in any previous study. Regarding just the azimuthal current components, the strongest currents appear in the pre-midnight and post-dawn quadrants. However, sampling differences make discerning trends in these plots difficult. Furthermore, the pure azimuthal component provides a misleading picture because it omits the strong Earthward components, as well as the z-component as seen in Figure 7.

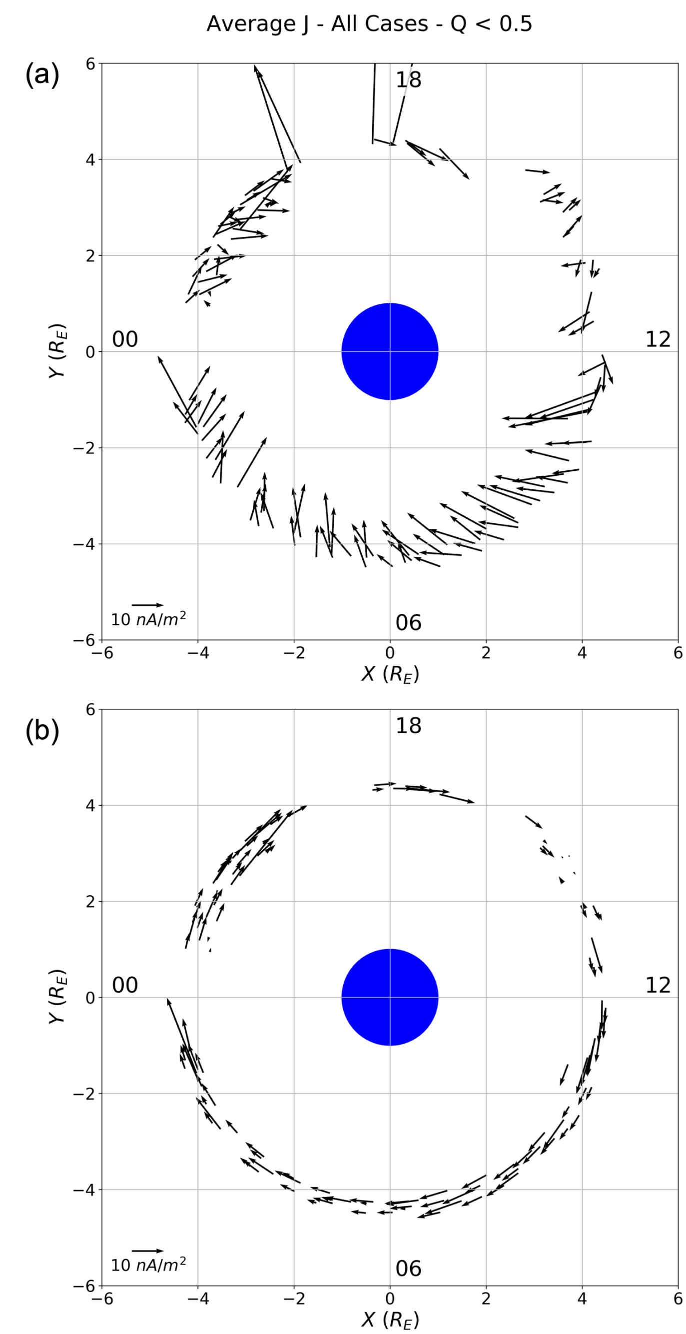

Figure 8. Current vectors averaged by orbit over Q < 0.5 for L < 7. **a)** Full current vectors in the x-y plane. Each vector is averaged about the magnetic equator for clarity. Note that this is a top-down view of Figure 7. **b)** Azimuthal current components of the vectors in (a).

Current magnitude seems to have weak dependence on local time according to Figure 8, with peaks in the post-dawn and pre-midnight sectors. For a clearer view, Figure 9 provides a scatter plot of individual data points from every orbit subject to Q < 0.5 and L < 7, this time without averaging. While the limited viable timeframe for each orbit still makes trends difficult to observe, there is a tendency towards strong currents before midnight. A closer examination reveals another less-dramatic increase in the post-dawn sector. Thus, the same trends are seen in both Figure 8 and Figure 9, even considering both disturbed and quiet events and before customized filtering.

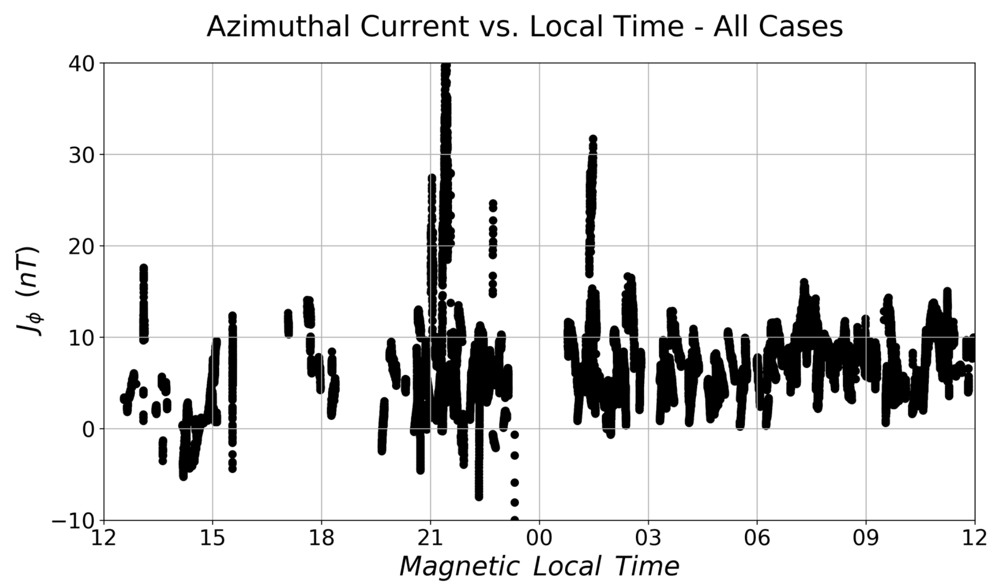

Figure 9. Azimuthal current over all local times. Data for this figure include all orbits, constrained to Q < 0.5 and L < 7.

While the above estimates provide methodically-consistent ring current computation, each case can be assessed individually to account for nonphysical output. For example, data from 2001 should be discarded because it does not usually show a clear transition to the ring current region, and because the tetrahedron characteristic size is larger than 1000 km. Additionally, data from the 2003-2004 orbits can sometimes be noisy or have large nonphysical trends that should be eliminated. Finally, the case from 18 March 2002 has been excluded because of the uniqueness of the observed current structure. This particular case is consistent with expected structure of a plasma nose, fortuitously captured by Cluster but not a desired observation of a typical ring current. The results of filtering are provided in Figure 10; note that it shows the same parameters as Figure 6.

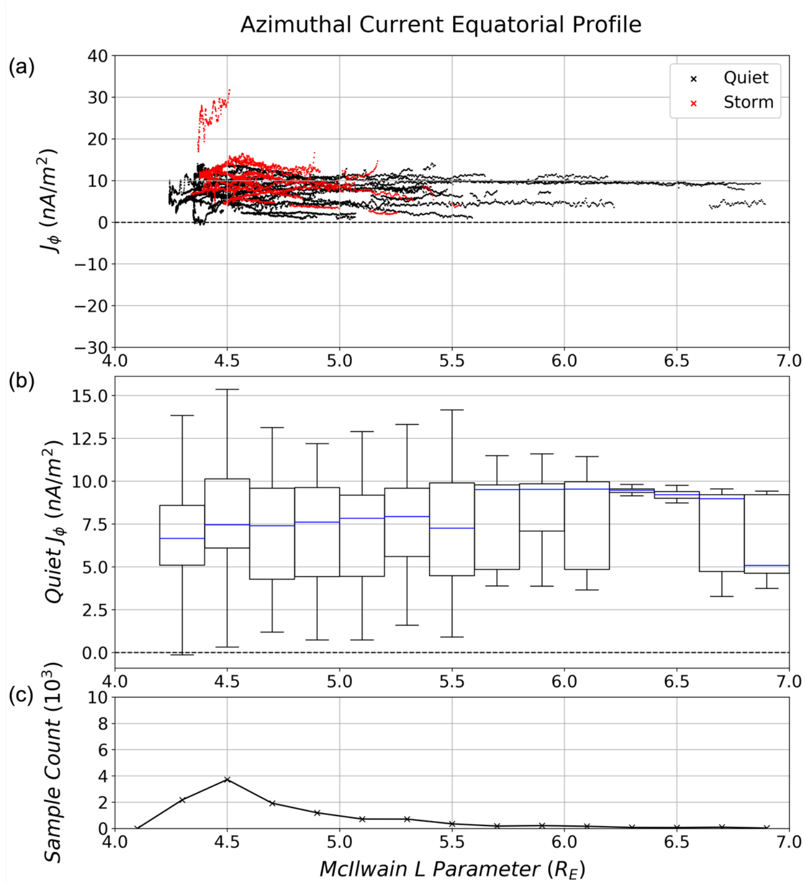

Figure 10. Data from filtered current events. **a)** Remaining azimuthal currents subject to Q < 0.5. **b)** Quiet data binned by L-shell, using identical format as Figure 6b. **c)** Quiet observation count per data bin. Note that the same bins contain fewer points than those in Figure 6c.

The filtered dataset is significantly smaller than the total, and the climatological study shows a different trend. The results now have a larger IQR for most L bins, and no longer extend as far Earthward. Thus, there is less confidence in the representativeness of this sample.

Figure 11 addresses the impacts of the ring current on the Earth's magnetic field by comparing the Cluster-derived currents and the Dst index. The data are filtered using the original scheme, subject to Q < 0.5 and L < 7, and the same Dst index is applied to the entire perigee pass. For this figure, only azimuthal current is considered. The data are then colored by L-shell. All data from each flight track are included, rather than averaging or taking the maximum current, because the observed current structures did not support good physical meaning of either measure. For example, many cases from 2003 had the maximum azimuthal current occur right at entry into the proposed ring current region, which is then subject to boundary interpretation and contradictory to theory.

Comparing azimuthal current to Dst does indeed show a correlation consistent with expectations; namely, increased current (as from a storm) decreases the Dst index. The lack of well-defined current maxima on each flight track combined with the spatial variability of the ring current itself obscure a concise relationship, but the observed correlation between Dst and azimuthal current does agree with results from other studies (eg., Zhang et al., 2011) and is contradictory to the initial Vallat et al. (2005) paper. Keep in mind that the selection criteria for the definition of ring current in this study is the diffusional component, not the convective component directly entering the inner magnetosphere from the plasma sheet and most likely responsible for the majority of the Dst perturbation.

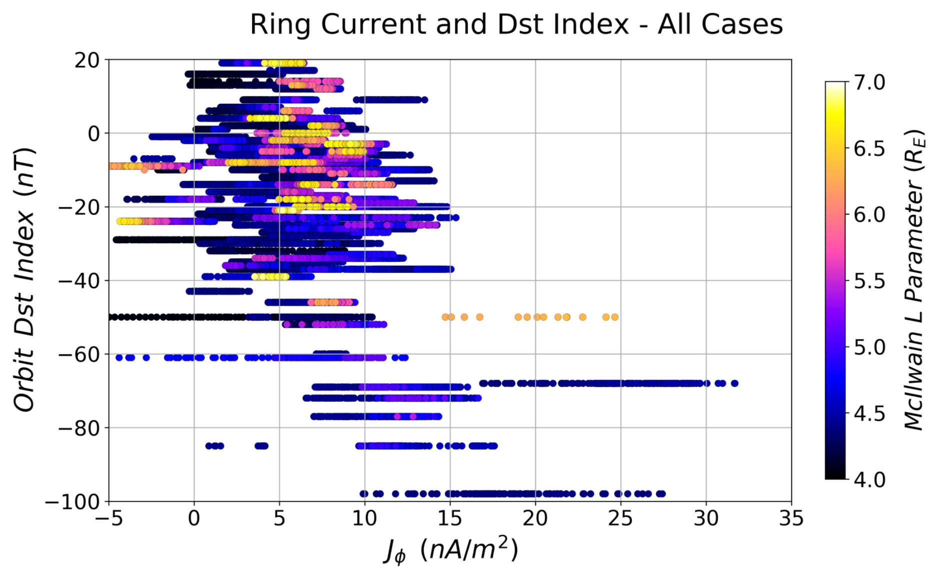

Figure 11. Azimuthal Current and event Dst Index. Here, the azimuthal current components where $Q < 0.5$ are compared to the Dst index averaged throughout the event timing. Each data point is colored by L-shell. Ring current strength has only weak correlation with Dst index according to Cluster data.

It can be concluded that, after filtering, Cluster curlometer output has limited climatological value for assessing the inner magnetosphere current density. There is more information contained in analysis of individual passes than in views of the system as a whole, but the sample size is too small to 'wash out' effects of a single pass or to show a robust trend. It is sufficient to note that the ring current is a highly-variable structure, in both magnitude and extent, and therefore small variations in the environment can lead to drastic changes. Geomagnetic indices do not have strong correlation ($r = -0.18$ at $L = 5$, $r = -0.31$ at $L = 4.5$) with ring current magnitude (Figure 11), so further analysis of events is required to show causal relationships.

5. Discussion

The curlometer technique has produced unexpected results in the discussed applications: simulated current environment, single perigee pass, and climatological study. In the simulated current environments, the curlometer calculation produced the imposed current with high fidelity in regular tetrahedra and where nonlinearities were constrained or eliminated. However, using actual spacecraft position data and a nonlinear magnetic environment that nevertheless preserved the quality parameter Q, false currents were detected by the curlometer that were not imposed in the simulation. Standing alone, this directly challenges the efficacy of Q but does not imply anything about the ring current itself. However, single perigee passes displayed unique current structures. The strong asymmetry of the current throughout the perigee passes, especially in the 2003 data where current components remained continuous without sudden spikes but diverged later in the flight track, casts doubt on the validity of the observed structure. Although much of the divergent current region lies outside of $Q < 0.5$ and is therefore untrustworthy, the trends begin well within the filtered data. Curlometry within $Q < 0.5$ should be symmetrical about the magnetic equator, since plasma bounces along field lines and therefore organizes by L-shell, but this symmetry is not seen. Instead, the diverging currents increase with tetrahedron irregularity, suggesting a causal relationship. In light of the simulated false currents, which also produce this divergence with tetrahedron irregularity, the single perigee passes all seem to contain some combination of poor tetrahedron quality or strong magnetic gradient that produces poor current estimates. This is bolstered by disagreement with plasma data.

Climatologies constructed using the curlometer are similarly unexpected. Currents are dominated by a large field-aligned component that is steadily southward in both the north and south hemispheres, and show only weak dependence on local time and Dst index. There is also a significant radial component Earthward at all local times. The ring current is expected to have a local peak in the pre-midnight sector, which is weakly observed in the Cluster data but without high confidence. Additionally, there are insufficient samples of storm-time ring current to estimate the effects of strong geomagnetic activity on the ring current strength and distribution. The most valuable climatological product is azimuthal current as a function of L-shell, which produces a consistent value for quiet-time ring current below 10 nA/m^2 and hints at a current reversal to the eastward ring current within $L = 4$. Although less steep than anticipated, the curlometer does detect a radial current peak. Attempts to clarify and sharpen these analyses by restricting data to stable, trustworthy, or expected structure for individual perigee passes using established quality indices were unsuccessful in refining the dataset. Therefore, the climatologies of the ring current using Cluster data must stand as presented here, including the unusual features and limitations.

6. Conclusions

Revisitation of Cluster ring current measurements has called into question the efficacy of the curlometer technique in this region. Individual time series plots show clear errors in current magnitude and direction, especially when the tetrahedron is distorted. Furthermore, extensive simulation shows that the parameter Q does not always accurately represent the current estimate quality, and at the accepted threshold of $Q < 0.5$ can produce false currents as large as 100% of the actual current. Lowering the threshold reduces the sample size to a highly-restricted domain that obscures sought trends. Previous current estimates of ~20 nA/m^2 are nevertheless not upheld by this study, with quiet cases overwhelmingly below 10 nA/m^2.

The discrepancy between legacy plasma moment estimates of ring current strength and distribution and Cluster curlometer values has narrowed significantly, with a newfound magnitude median peaking at just 7 nA/m^2. The new analysis presented above finds that the ring current is weaker during the 2002-2004 period than previous estimates, and within reasonable ranges of plasma pressure gradient even before event filtering. Climatologies using these data should nevertheless be extremely cautious of the quality of current estimates, and effectively removing unsatisfactory cases reduces the sample size to preclude judgment on large-scale trends.

Thus, any work that relies on Cluster ring current data, including magnitudes and climatologies, should be viewed with full knowledge of the caveats and limitations described herein. Although shortcomings in curlometry are discussed in detail here, the extent of this analysis is restricted to Cluster spacecraft within the specified orbits and around perigee. The use of curlometry elsewhere should be examined for similar effects, but the uncertainties in the ring current region cannot be directly applied to other regions because of the strong dependence on magnetic field nonlinearity and tetrahedron shape/orientation.

Acknowledgments and Data

This project was funded in part through a grant from the National Science Foundation's Research Experience for Undergraduates Program (Grant Number 1659248) and NSF grant 1663770, as well as by NASA grants 80NSSC17K0015 and NNX17AB87G. The authors give special thanks to the developers and curators of the SpacePy Python package, which proved invaluable for coordinate conversions and data processing. We would also like to acknowledge Dr. Michael Hirsch for use of his Python igrf12 package. DOI: 10.5281/zenodo.3461075. Cluster magnetometer data used in this study are available at the Cluster Science Archive (https://csa.esac.esa.int/csa-web/) and the simulated data sets and Python code are available at the University of Michigan Deep Blue data repository (https://deepblue.lib.umich.edu/data). We will "mint a DOI" to finalize and freeze the data brick upon acceptance.

References

Balogh, A., Carr, C. M., Acuña, M. H., Dunlop, M. W., Beek, T. J., Brown, P., et al. (2001). The Cluster Magnetic Field Investigation: overview of in-flight performance and initial results. *Annales Geophysicae*, 19(10/12), 1207–1217. https://doi.org/10.5194/angeo-19-1207-2001.

Daly, P. W., & Kronberg, E. A. (2013). User Guide to the RAPID Measurements in the Cluster Science Archive (CSA) (5.4). Goettingen, Germany.

Dandouras, I., & Barthe, A. (2011). User Guide to the CIS measurements in the Cluster Active Archive (CAA) (Vol. 2.0).

Dandouras, I., & Barthe, A. (2015). Cluster Active Archive: Interface Control Document for CIS.

Dunlop, M. W., Balogh, A., Glassmeier, K.-H., & Robert, P. (2002). Four-point Cluster application of magnetic field analysis tools: The Curlometer. *Journal of Geophysical Research*, 107, 1384. DOI:10.1029/2001JA005088

Dunlop, M. W., Haaland, S., Dong, X. C., Middleton, H. R., Escoubet, C. P., Yang, Y. Y., et al. (2018). Multipoint analysis of electric currents in geospace using the curlometer technique. *Electric Currents in Geospace and Beyond*, 67–80. https://doi.org/10.1002/9781119324522.ch4.

Dunlop, M. W., Haaland, S., Escoubet, P. C., & Dong, X.-C. (2016). Commentary on accessing 3-D currents in space: Experiences from Cluster. *Journal of Geophysical Research: Space Physics*, 121(8), 7881–7886. https://doi.org/10.1002/2016JA022668.

Dunlop, M. W., Southwood, D. J., Glassmeier, K. H., & Neubauer, F. M. (1988). Analysis of multipoint magnetometer data. *Advances in Space Research*, 8(9–10), 273–277. https://doi.org/10.1016/0273-1177(88)90141-X.

Dunlop, M. W., Yang, J. Y., Yang, Y. Y., Xiong, C., Lühr, H., Bogdanova, Y. V., et. al (2015). Simultaneous field-aligned currents at Swarm and Cluster satellites. *Geophysical Research Letters*, 42(10), 3683–3691. https://doi.org/10.1002/2015GL063738.

Fränz, M., & Harper, D. (2002). Heliospheric coordinate systems. *Planetary and Space Science*, 50(2), 217–233. https://doi.org/10.1016/S0032-0633(01)00119-2.

Ganushkina, N. Y., Liemohn, M. W., Dubyagin, S., Daglis, I. A., Dandouras, I., DeZeeuw, D. L, et. al (2015). Defining and resolving current systems in geospace. *Annales Geophysicae*, 33, 1269-1402. doi:10.5194/angeo-33-1369-2015

Ganushkina, N. Y., Liemohn, M. W., & Dubyagin, S. (2018), Current systems in the Earth's magnetosphere, *Reviews of Geophysics*, *56*(2), 309-332, doi: 10.1002/2017RG000590.

Greenspan, M. E., & Hamilton, D. C. (2000). A test of the Dessler-Parker-Sckopke relation during magnetic storms. *Journal of Geophysical Research Space Physics, 105*, 5419-5430.

Grimald, S., Dandouras, I., Robert, P., & Lucek, E. (2012). Study of the applicability of the curlometer technique with the four Cluster spacecraft in regions close to Earth. *Annales Geophysicae*, 30(3), 597–611. https://doi.org/10.5194/angeo-30-597-2012.

Hapgood, M. A. (1992). Space physics coordinate transformations: A user guide. Planetary and Space Science, 40(5), 711–717. https://doi.org/10.1016/0032-0633(92)90012-D.

Henderson, P. D., Owen, C. J., Lahiff, A. D., Alexeev, I. V., Fazakerley, A. N., Yin, L., et al. (2008). The relationship between $j \times B$ and $\nabla \cdot Pe$ in the magnetotail plasma sheet: Cluster observations. *Journal of Geophysical Research: Space Physics*, 113(7), 1–17. https://doi.org/10.1029/2007JA012697.

Laakso, H., Perry, C., McCaffrey, S., Herment, D., Allen, A. J., Harvey, C. C., et al. (2010). Cluster Active Archive: Overview. In H. Laakso et al. (Ed.), *Astrophysics and Space Science Proceedings* (pp. 3–37).

Le, G., Russell, C. T., & Takahashi, K. (2004). Morphology of the ring current derived from magnetic field observations. *Annales Geophysicae*, 22, 1267-1295. 10.5194/angeo-22-1267-2004.

Liemohn, M. W., Kozyra, J. U., Thomsen, M. F., Roeder, J. L., Lu, G., Borovsky, J. E., & Cayton, T. E. (2001). Dominant role of the asymmetric ring current in producing the stormtime Dst*, *Journal of Geophysical Research*, 106, 10883-10904. DOI:10.1029/2000JA000326.

Liemohn, M. W., Kozyra, J. U., Clauer, C. R., & Ridley, A. J. (2001). Computational analysis of the near-Earth magnetospheric current system, *Journal of Geophysical Research*, 106, 29,531, 2001. DOI: 10.1029/2001JA000045.

Liemohn, M. W., Katus, R. M., & Ilie, R. (2015), Statistical analysis of storm-time near-Earth current systems, *Annales Geophysicae, 33*, 965-982, doi: 10.5194/angeo-33-965-2015.

Liemohn, M. W., Ganushkina, N. Y., Ilie, R., & Welling, D. T. (2016). Challenges associated with near-Earth nightside current. *Journal of Geophysical Research: Space Physics*, 121, 6763–6768. https://doi.org/10.1002/2016JA022948.

Lui, A. T. Y., & Hamilton, D. C. (1992). Radial profiles of quiet time magnetospheric parameters. *Journal of Geophysical Research*, 97(A12), 19325. https://doi.org/10.1029/92ja01539.

Lui, A. T. Y., McEntire, R.W., & Krimigis, S. M. (1987). Evolution of the ring current during two geomagnetic storms. *Journal of Geophysical Research*, 92, 7459–7470.

Middleton, H., & Masson, A. (2016). The Curlometer technique: a beginner's guide. ESDC-CSA-TN-0001 (Vol. 1).

Milillo, A., Orsini, S., & Daglis, I. A. (2001). Empirical model of proton fluxes in the equatorial inner magnetosphere: Development. *Journal of Geophysical Research Space Physics, 106*, 25,713-25,729.

Milillo, A., Orsini, S., Delacourt, D. C., Mura, A., Massetti, S., De Angelis, E., & Ebihara, Y. (2003), Empirical model of proton fluxes in the equatorial inner magnetosphere: 2. Properties and applications, *Journal of Geophysical Research Space Physics*, 108, A5. 1165// https://doi.org/10.1029/2002JA009581

Paschmann, G., & Daly, P. W. (2000). Analysis Methods for Multi-Spacecraft Data. ISSI Scientific Report.

Petrukovich, A., Artemyev, A., Vasko, I., Nakamura, R., & Zelenyi, L. (2015). Current Sheets in the Earth Magnetotail: Plasma and Magnetic Field Structure with Cluster Project Observations. *Space Science Reviews*, 188(1–4), 311–337. https://doi.org/10.1007/s11214-014-0126-7.

Reme, H., Bosqued, J. M., Sauvaud, J. A., Cros, A., Dandouras, J., Aoustin, C., et al. (1997). The Cluster Ion Spectrometry (CIS) Experiment. *Space Science Reviews*, 79, 303–350. Retrieved from http://www.space.irfu.se/exjobb/2003_erik_bergman/articles/CIS.pdf

Robert, P., Dunlop, M. W., Roux, A., & Chanteur, G. (1998). Reprinted from Analysis Methods for Multi-Spacecraft Data Accuracy of Current Density Determination 16.1 Introduction. In G. Paschmann & P. W. Daly (Eds.), Analysis Methods for Multi-Spacecraft Data (1.1, pp. 395–418). ISSI/ESA.

Sergis, N., Krimigis, S. M., Mitchell, D. G., Hamilton, D. C., Krupp, N., Mauk, B. M., et al. (2007). Ring current at Saturn: Energetic particle pressure in Saturn's equatorial magnetosphere measured with Cassini/MIMI. *Geophysical Research Letters*, 34(9), 1–6. https://doi.org/10.1029/2006GL029223.

Shen, C., Yang, Y. Y., Rong, Z. J., Li, X., Dunlop, M., Carr, C. M., et al. (2014). Direct calculation of the ring current distribution and magnetic structure seen by Cluster during geomagnetic storms. *Journal of Geophysical Research: Space Physics*, 119(4), 2458–2465. https://doi.org/10.1002/2013JA019460.

Vallat, C., Dandouras, I., Dunlop, M., Balogh, A., Lucek, E., Parks, G. K., et al. (2005). First current density measurements in the ring current region using simultaneous multi-spacecraft CLUSTER-FGM data. *Annales Geophysicae*, 23(5), 1849–1865. https://doi.org/10.5194/angeo-23-1849-2005.

Zhang, Q. H., Dunlop, M. W., Lockwood, M., Holme, R., Kamide, Y., Baumjohann, W., et al. (2011). The distribution of the ring current: Cluster observations. *Annales Geophysicae*, 29(9), 1655–1662. https://doi.org/10.5194/angeo-29-1655-2011.